Nucl. Fusion **49** (2009) 085011 (13pp) doi:10.1088/0029-5515/49/8/085011

Physics of penetration of resonant magnetic perturbations used for Type I edge localized modes suppression in tokamaks

M. Bécoulet[1], G. Huysmans[1], X. Garbet[1], E. Nardon[2], D. Howell[2], A. Garofalo[3], M. Schaffer[3], T. Evans[3], K. Shaing[4,5], A. Cole[4], J.-K. Park[6] and P. Cahyna[7]

[1] CEA, IRFM, F-13108, St-Paul-lez-Durance, France
[2] Euratom/UKAEA Fusion Association, Culham Science Centre, Abingdon OX143DB, UK
[3] General Atomics, PO Box 85608, San Diego, CA 92186-5688, USA
[4] University of Wisconsin, Madison, WI 53706-1609, USA
[5] Plasma and Space Science Center and Physics Department, National Cheng Kung University, Tainan, Taiwan 70101, Republic of China
[6] Princeton Plasma Physics Laboratory, Princeton, NJ 08543, USA
[7] Institute of Plasma Physics ASCR, v.v.i., Association EURATOM/IPP.CR, Za Slovankou 3, 18200 Prague, Czech Republic

Received 13 January 2009, accepted for publication 29 May 2009
Published 17 July 2009
Online at stacks.iop.org/NF/49/085011

Abstract
Non-linear reduced MHD modelling of the toroidally rotating plasma response to resonant magnetic perturbations (RMPs) is presented for DIII-D and ITER-like typical parameter and RMP coils. The non-linear cylindrical reduced MHD code was adapted to take into account toroidal rotation and plasma braking mechanisms such as resonant one ($\sim j \times B$) and the neoclassical toroidal viscosity (NTV) calculated for low collisionality regimes ('$1/\nu$' and 'ν'). Counter toroidal rotation by NTV is predicted for ITER with the proposed RMP coils in $1/\nu$-limit. Resonant braking is localized near resonant surfaces and is weak compared with NTV in the $1/\nu$ regime for typical DIII-D and ITER parameters. Toroidal rotation leads to the effective screening of RMPs that is larger for stronger rotation and lower resistivity, resulting mainly in central islands screening. Non-resonant helical harmonics ($q \neq m/n$) in RMP spectrum are not influenced by plasma rotation, and hence penetrate and are important in NTV mechanism.

PACS numbers: 52.55Fa, 52.65Kj

(Some figures in this article are in colour only in the electronic version)

1. Introduction

During the recent design review of ITER, Type I edge localized mode (ELM) control was identified as a high priority task [1]. One of the promising methods to control Type I ELMs is the installation of dedicated coils that achieve this goal by modifying the edge magnetic field, so-called resonant magnetic perturbation (RMP) coils. RMPs have been shown to be effective in eliminating Type I ELMs in DIII-D [2] or significantly mitigating them [3] in JET. At present, ELM control by RMP is recommended for ITER since it could increase the lifetime of the ITER divertor by reducing heat and particle fluxes due to Type I ELMs and hence reducing surface erosion [1]. Present day experiments on ELM control by RMP are not completely understood. The extrapolations to ITER are mainly based on an empirical criterion and 'vacuum' field modelling, suggesting that ELMs are suppressed when the edge plasma is ergodized in the pedestal region for $r/a \sim \sqrt{\psi_{\rm pol}} > 0.9$, where $\psi_{\rm pol}$ is a poloidal magnetic flux. This criterion is also used for the design of the RMP coils for ITER [4, 5]. However, depending on the plasma parameters and the RMP spectrum, the actual RMP field could be very different, especially in rotating plasmas where the generation of the current perturbations near rational surfaces could prevent reconnections, leading to the effective screening of RMPs [6–8]. On the other hand, it is known from experiment

that helical magnetic perturbations can significantly influence the toroidal rotation itself [2, 3, 7–10]. In most experimental cases slowing down of the global plasma rotation is observed, potentially leading, in particular in the cases with low n toroidal symmetry ($n = 1$–2), to core MHD mode locking and disruptions [3, 8–10]. However, the physics of toroidal plasma rotation with RMPs is more complicated: in some experiments a local increase in the toroidal rotation at the pedestal was observed [2] and, moreover, at weak co- and counter rotation acceleration in the counter direction was demonstrated [10]. The neoclassical toroidal viscosity (NTV), resulting from the toroidal drag force experienced by the plasma particles moving along field lines distorted by helical magnetic perturbations [11–14], was proposed as a possible mechanism for the global plasma braking. However, many open questions remain in the experimental confirmation [8–10] of NTV mechanism, since the theoretically estimated NTV force [11–14] depends strongly on plasma parameters and, in particular, on the plasma collisionality and rotation which can change significantly the RMP spectrum in plasma compared with the vacuum fields. The helical perturbations can appear due to the intrinsic MHD activity (resistive wall modes, tearing modes, etc) or external magnetic perturbations such as RMPs. NTV is produced due to any helical magnetic perturbation, including both the resonant ($q = m/n$) and non-resonant parts ($q \neq m/n$) of the perturbation spectrum [8–14]. The understanding of the rotating plasma response on RMPs is important in the optimization of the RMP coil spectrum. The loss of the plasma co-rotation due to NTV can be important in ITER, where the expected toroidal rotation is already slow (∼1 kHz) compared with the existing experiments (∼10 kHz) [2–4, 10]. However, as predicted by neoclassical theory [13], strong NTV does not slow plasma rotation down to zero, but to a so-called offset rotation in the counter direction and on the order of the ion diamagnetic frequency, as was seen experimentally on DIII-D [10].

This paper describes recent results based on the non-linear reduced MHD modelling of RMPs in rotating plasmas for DIII-D and ITER parameters. In section 2 the reduced MHD (RMHD) model with toroidal plasma rotation and different plasma braking mechanisms is introduced for cylindrical geometry. In section 3 the NTV models for low collisionality regimes are presented. The corresponding numerical estimations for DIII-D and ITER typical parameters and RMP coils (I-coils for DIII-D [2] and ITER ELM control coils [1, 4, 5]) are given. Section 4 describes main results on rotating plasma response to RMPs calculated by the code RMHD. In the appendix the recipe for calculation of the magnetic perturbation spectrum in the Hamada coordinates needed for NTV theory application is given.

2. Reduced MHD model with RMPs

The non-linear cylindrical RMHD code [15] was adapted to take into account toroidal plasma rotation, resonant braking [6–8] and NTV [11–14]. More details about the derivation, ordering and conservation laws for this four-field non-linear RMHD model with parallel flows are given in [16]. The equations solved here, normalized as in [15], are

$$\frac{\partial \psi}{\partial t} + v_z \frac{\partial \psi}{\partial z} + \nabla_\parallel \Phi = -\eta j, \tag{2.1}$$

$$\frac{\partial W}{\partial t} + v_z \frac{\partial W}{\partial z} + \nabla_\parallel j + [\Phi, W] = \nu_{0,\perp} \nabla^2 W, \tag{2.2}$$

$$\frac{\partial v_z}{\partial t} + v_z \frac{\partial v_z}{\partial z} + [\Phi, v_z] + \vec{\nabla}_\parallel p = S_v + \nu_{0,\parallel} \nabla^2 v_z + F_{\mathrm{RB}} + F_{\mathrm{NTV}}, \tag{2.3}$$

$$\frac{\partial p}{\partial t} + v_z \frac{\partial p}{\partial z} + [\Phi, p] = k_\perp \nabla^2 p + S_p. \tag{2.4}$$

Here $\psi = \psi_0 + \tilde{\psi}$ is the poloidal flux. Identifying equilibrium values with 'eq' and perturbations with '∼', the total magnetic field is represented as follows:

$$\vec{B} = \vec{B}_{\mathrm{eq}} + \tilde{\vec{B}}, \quad \tilde{\vec{B}} = \left(\frac{1}{r} \frac{\partial \tilde{\psi}}{\partial \theta}; -\frac{\partial \tilde{\psi}}{\partial r}; 0 \right),$$

$$\vec{B}_{\mathrm{eq}} \approx B_0 (0, b_{\theta,0}(r), b_{z,0}), \qquad b_{z,0} \approx b_0 = 1,$$

$$b_{\theta,0}(r) = -\frac{1}{B_0} \frac{\partial \psi_0}{\partial r}.$$

Other variables are Φ is the electrostatic potential, $W = -\nabla^2 \Phi$ is the vorticity, p is the pressure, $\vec{v} = \vec{v}_\perp + \vec{v}_\parallel$ is the total velocity where the component parallel to the equilibrium magnetic field is approximated as $\vec{v}_\parallel = \vec{b}_{\mathrm{eq}}(\vec{v}, \vec{b}_{\mathrm{eq}})$, $\vec{b}_{\mathrm{eq}} = \vec{B}_{\mathrm{eq}}/B_{\mathrm{eq}}$, $v_z \approx V_\varphi$ is the toroidal velocity and the poloidal velocity is approximated as $\vec{v}_\perp \approx -(\vec{\nabla}\Phi \times \vec{e}_z)$, $k_\perp$ is the diffusion coefficient, $\nu_{0,\perp}$, $\nu_{0,\parallel}$ are perpendicular and parallel viscosities, $j = -\nabla^2 \psi$ is toroidal current, and $B_0 = 1$ is the normalized magnetic field on the axis. To derive the induction equation (2.1) we used the projection on the equilibrium field:

$$(-\nabla\Phi - (\partial\psi \vec{e}_z/\partial t) - \eta \vec{J}) \cdot \vec{b}_{\mathrm{eq}} \approx -\left(\vec{v}_\perp \times \vec{B} + \vec{v}_\parallel \times \tilde{\vec{B}} \right) \cdot \vec{b}_{\mathrm{eq}};$$

note that

$$\left(b_{0,\theta} v_{\parallel,z}/r \right) (\partial\psi/\partial\theta) = -v_{\parallel,z} \left(\partial\psi/\partial z \right),$$

where the cylindrical safety factor is

$$q(r) = \frac{r b_{z,0}}{R_0 b_{\theta,0}}, \qquad b_{z,0} = 1 \quad \text{and} \quad 1/R_0 \partial_\varphi \ldots = \partial_z \ldots.$$

The equilibrium flow is given by $\vec{v}_0 = (0, v_{\theta,0}, v_{z,0})$, $v_{\theta,0} \ll v_{z,0}$. $S_{p,v}$ represents sources that are adjusted to keep initial equilibrium profiles in the case without RMPs. The initial toroidal rotation profile is parabolic with zero value at the boundary: $V_z(t, r = 1) = 0$. In the present modelling the pressure terms were neglected by setting the normalized pressure small: $p \sim 10^{-6}$. Curvature and diamagnetic effects are also not included in this version of the cylindrical code. The reason for this limit is that ballooning modes are always unstable in cylindrical geometry and hence the realistic toroidal geometry is essential. The present cylindrical approximation allows a description of the forced reconnections and current instabilities (tearing and kink modes triggering). As far as possible amplification of RMPs is concerned, only current profile instabilities (however, not observed in the present modelling with the current profiles used here) can be modelled in this approximation. The cylindrical code RMHD represents an advantage that low experimental-like resistivity plasmas

(Lindquist number up to $S_{\max} \sim 10^9$) and more realistic toroidal rotation evolution can be modelled compared with our previous work [17], where non-linear modelling of RMPs in a torus with rigid body rotation was done, but at $S_{\max} \sim 10^6$. However, note that this RMHD model does not allow resistive ballooning mode destabilization and, hence, possible amplification of RMPs [20] by this mechanism, which will be a subject of our future work.

The parallel gradient is $\nabla_\parallel .. = \partial../\partial z + [.., \psi]$ and the brackets are defined as $[\Phi, \psi] = \vec{e}_z \cdot \nabla_\perp \Phi \times \nabla_\perp \psi$. Identifying physical parameters by superscript (ph), the normalized parameters used in the code are defined as follows:

$$B^{\rm ph} = B_{0,z} B \equiv B_0 B; \quad \psi^{\rm ph} = a B_0 \psi; \quad r^{\rm ph} = a r;$$
$$R_0^{\rm ph} = a R_0; \quad \rho^{\rm ph} = \rho_0 \rho = \rho_0 = \text{const}$$
$$v^{\rm ph} = V_{\rm A} v = \frac{B_0}{\sqrt{\mu_0 \rho_0}} v; \quad t^{\rm ph} = \tau_{\rm A} t; \tag{2.5}$$
$$\tau_{\rm A} = \frac{a}{V_{\rm A}}; \quad \Phi^{\rm ph} = \frac{a B_0^2}{\sqrt{\mu_0 \rho_0}} \Phi;$$
$$p^{\rm ph} = \frac{B_0^2}{\mu_0} p; \quad \eta^{\rm ph} = \frac{a B_0 \sqrt{\mu_0}}{\sqrt{\rho_0}} \eta; \quad \nu^{\rm ph}_{0,(\parallel,\perp)} = \frac{a^2}{\tau_{\rm A}} \nu_{0,(\parallel,\perp)}.$$

All variables are represented in Fourier series, for example poloidal flux $\psi = \sum_{m,n=\pm\infty} \psi_{nm} e^{im\theta + inz/R_0}$ + c.c., and the harmonic $n = 0, m = 0$ is the equilibrium value. The boundary conditions at $r = 1$ are zero for all perturbations except for the magnetic flux harmonic amplitudes, $\psi_{nm}|_{r=1} \approx \psi^{\rm vac}_{nm,\rm sep}$, which are approximated by the vacuum amplitudes calculated in the toroidal geometry [4]. Note, however, that because of the much stronger magnetic shear in toroidal geometry, the amplitudes of the cylindrical harmonics at the edge were adjusted to satisfy edge islands overlapping (Chirikov parameter > 1) for $r > 0.9$ for the zero rotation case to correspond in this respect with the vacuum modelling in a torus [4]. Here for estimations we take $r \approx \sqrt{\psi_{\rm pol}}$. The resonant braking term due to $\vec{j} \times \vec{B}$ forces in (2.3) is taken into account only for the mean flow ($n = 0, m = 0$) as in [7, 8]:

$$F^{00}_{\rm RB} = \frac{-1}{2q R_0} \text{Im} \sum_{m,n\neq 0} m \left[j_{nm} \psi^*_{nm} - \Phi_{nm} \left(\frac{\partial \Phi^2_{nm}}{\partial r^2} - \frac{1}{r} \frac{\partial \Phi_{nm}}{\partial r} \right)^* \right]. \tag{2.6}$$

However, let us note already that, for the typical RMP amplitudes modelled here, the resonant braking (2.6) typically localized near the resonant surfaces [6–8] is very small (see section 4).

3. Modelling of NTV in DIII-D and ITER

The expression for the neoclassical toroidal viscous force [11–14] is taken from [13]:

$$F_{\rm NTV} = -\nu^\parallel_{\rm eff} b^2_{\rm eff} \left(V_\varphi - V^{\rm NC}_\varphi \right) \approx -\alpha_{\rm NTV}(r) \left(V_\varphi - V^{\rm NC}_\varphi \right). \tag{3.1}$$

Here $\nu^\parallel_{\rm eff}$ is the effective frequency, $b^2_{\rm eff}$ is the square of the effective magnetic perturbation calculated in the Hamada coordinates in a specific way depending on the collisionality

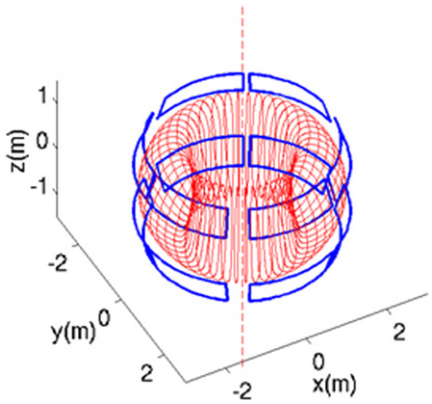

Figure 1. Sketch of two rows of six I-coils in DIII-D with schematic view of plasma flux surfaces.

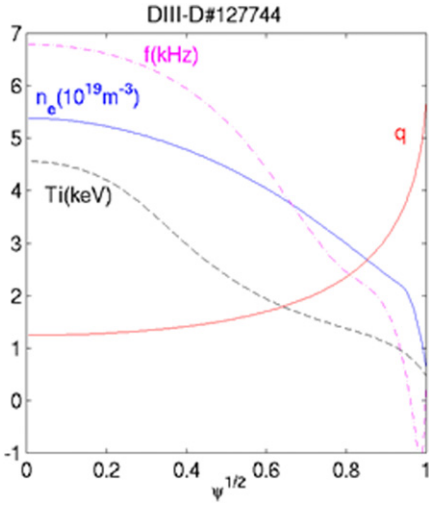

Figure 2. DIII-D shot #127744 profiles used for NTV estimations.

regime [11–14], V_φ is the toroidal velocity and $V^{\rm NC}_\varphi$ is the neoclassical toroidal velocity in a helically perturbed magnetic field introduced in [13]. Since the realistic toroidal geometry is very important for the NTV estimations [7–9], we stepped out from the self-consistency in RMHD modelling with NTV and used flux-averaged $\alpha_{\rm NTV}(r)$ calculated in toroidal geometry as an input without changing it in time. In this paper the magnetic perturbation in the NTV calculations was taken in vacuum as a starting hypothesis neglecting plasma response.

For DIII-D I-coils (figure 1), the DIII-D #127744 discharge profiles of figure 2 were used with $B_0 = 1.9\,$T, $R_0 = 1.8\,$m, $a = 0.6\,$m, $n = 3$, $I_{\rm coil} = 4.65\,$kAt and odd parity phasing, corresponding to the anti-symmetric current signs in the upper and lower rows of I-coils.

For the ITER cases the geometry of the latest design of 9×3-rows in-vessel RMP coils [1] (figure 3) were modelled by zero-thickness equally spaced frames with $\sim 26^\circ$ toroidal width. The corner coordinates (R, Z) in (m) for the top coil are (7.71; 3.35);(8.53; 1.87); mid: (8.73; 1.75); (8.73; −0.5); bottom coil: (8.55; −0.62);(7.45; −2.49). The dominant toroidal number in the ITER coils spectrum was $n = 4$, produced by currents (in kAt) approximating $n = 4$ sinusoids in the top row: (−49.9; 45.675; −35.95; 21.9; −5.225; −12.1; 27.95; −40.45; 48.05); the mid-row: (50; −47; 38.3; −25;

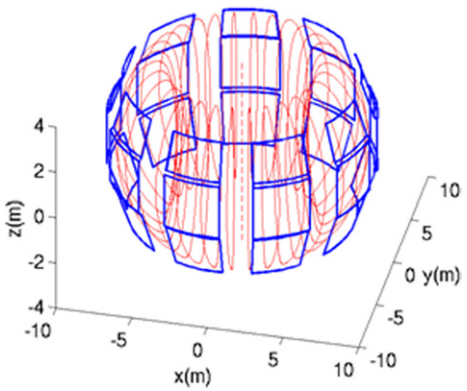

Figure 3. Sketch of three rows of nine ITER RMP in-vessel coils with plasma flux surfaces.

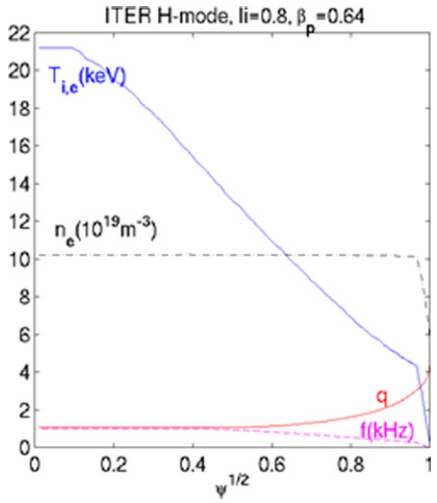

Figure 4. ITER H-mode profiles from [24] used for NTV estimations.

8.7; 8.7; −25; 38.3; −47) and the bottom row: (−42.4; 48.9; −49.5; 44.15; 33.45; 18.75; −1.75; −15.45; 30.8). The ITER standard H-mode scenario parameters ($B_0 = 5.29\,\mathrm{T}$, $R_0 = 6.2\,\mathrm{m}$, $a = 1.98\,\mathrm{m}$, $q_{95} \sim 3$) are the same as used in [4, 5]. The corresponding plasma profiles are presented in figure 4. The low collisionality '$1/\nu$' NTV regime is applicable according to [13] when $q\omega_E < \nu_\mathrm{i}/\varepsilon < \sqrt{\varepsilon}\omega_\mathrm{ti}$. Here $\varepsilon = r/R_0$, $\omega_E \approx E_r/(rB_\varphi)$ is the poloidal drift frequency, $\omega_\mathrm{ti} = V_\mathrm{ti}/(R_0 q)$ is the ion transit frequency and V_ti is the ion thermal velocity, as introduced in [13]. To estimate the radial electric field, the force balance equation was used:

$$E_r = \nabla_r P_\mathrm{i}/(eZ_\mathrm{i}n_\mathrm{i}) + V_\varphi B_\theta - V_\theta B_\varphi, \tag{3.2}$$

where the poloidal velocity is taken as neoclassical: $V_\theta = V_\theta^\mathrm{neo} \approx 1.17/(Z_\mathrm{i}B_\varphi)\mathrm{d}T_\mathrm{i}/\mathrm{d}r$ and $\nu_\mathrm{i} = 15.2/\sqrt{A}\ln\Lambda n_{(10^{19}\,\mathrm{m}^{-3})} T_{\mathrm{i(keV)}}^{-3/2}$ [13]. Note, however, the limits of the simplified formula for the equilibrium radial electric field which could be different especially in the pedestal region where the direct ion-orbit losses are important for the self-consistent estimations of E_r [18].

In the $1/\nu$ regime [13]

$$\begin{aligned}
&F_\mathrm{NTV} = -\nu_{1/\nu}^{\parallel} b_{1/\nu}^2 (V_\varphi - V_{1/\nu}^\mathrm{NC}),\\
&V_{1/\nu(\mathrm{m\,s^{-1}})}^\mathrm{NC} = 3.5/(Z_\mathrm{i}B_\theta)(\mathrm{d}T_{\mathrm{i,keV}}/\mathrm{d}r),\\
&\nu_{1/\nu}^{\parallel} = \omega_\mathrm{ti}^2/\nu_\mathrm{i},\\
&b_{1/\nu}^2 \approx 1.74 q^2 \varepsilon^{3/2} \sum_{n>0} \sum_{m,m'=\pm\infty} n^2\\
&\quad \times (b_{nmc} b_{nm'c} + b_{nms} b_{nm's}) W L_{nmm'},
\end{aligned} \tag{3.3}$$

where $b_{nmc,s}$ are the harmonic amplitudes of the field perturbation strength: $b \approx (\vec{B}_\mathrm{eq} \cdot \tilde{\vec{B}})/B_0^2$ in the Hamada coordinates, normalized to the magnetic field on the axis (B_0). The total magnetic field strength [11–14] is defined as $B = (\vec{B}_\mathrm{eq} + \tilde{\vec{B}}, \vec{B}_\mathrm{eq} + \tilde{\vec{B}})^{1/2} \approx B_\mathrm{eq} + B_0 b$. Introducing the label of the magnetic line, $\zeta^0 = q\theta^\mathrm{H} - \zeta^\mathrm{H}$, where $(\theta^\mathrm{H}, \zeta^\mathrm{H})$ are angles in the Hamada coordinates $(V^\mathrm{H}, \theta^\mathrm{H}, \zeta^\mathrm{H})$ introduced in [11, 12] and in the appendix of this paper, one can represent

$$\begin{aligned}
b &= \sum_{n=\pm\infty} \sum_{m=\pm\infty} b_{nm}^\mathrm{H} \mathrm{e}^{-\mathrm{i}n\zeta^\mathrm{H} + \mathrm{i}m\theta^\mathrm{H}}\\
&= \sum_{n>0} A_n \cos\left(n\zeta^0\right) + B_n \sin\left(n\zeta^0\right),
\end{aligned} \tag{3.4}$$

where

$$A_n = \sum_{m=\pm\infty} b_{nmc}\cos(\theta^\mathrm{H}(m - nq)) + b_{nms}\sin(\theta^\mathrm{H}(m - nq));$$

$$B_n = \sum_{m=\pm\infty} b_{nms}\cos(\theta^\mathrm{H}(m - nq)) - b_{nmc}\sin(\theta^\mathrm{H}(m - nq))$$

$$b_{nmc} = \begin{cases} 2\mathrm{Re}(b_{nm}^H), & m \neq 0,\\ \mathrm{Re}(b_{nm}^H), & m = 0, \end{cases}$$

$$b_{mns} = \begin{cases} -2\mathrm{Im}(b_{nm}^\mathrm{H}), & m \neq 0,\\ -\mathrm{Im}(b_{nm}^\mathrm{H}), & m = 0. \end{cases} \tag{3.5}$$

Note that usually in vacuum modelling for RMP coils [4, 5] another magnetic flux coordinate system with straight magnetic lines was used, where the toroidal angle is the geometrical one, and hence this system is not the Hamada coordinate system. Note also that here in section 3 the convention for resonant harmonics is taken from [11–13] $n > 0, m > 0, q_\mathrm{res} = m/n > 0$, which is different from the RMHD code [15] and section 2 where $q_\mathrm{res} = -m/n > 0, m > 0, n < 0$. However, since the results of section 3 are used as an average over flux surfaces and sums over all harmonic expressions in RMHD, we kept the different conventions as in the original papers for RMHD [15] and for NTV [11–13]. The definitions and all details of the procedure of changing of coordinates system and coefficients (3.5) calculation in the Hamada coordinates are presented in the appendix of this paper. The expressions for the weighting functions in the $1/\nu$ regime are

$$W_{nmm'} = \int_0^1 \frac{F_{nmc} F_{nm'c}\mathrm{d}k^2}{E(k) - (1 - k^2)K(k)},$$

$$F_{mnc}(k) = 2\int_0^{2\arcsin k} \sqrt{k^2 - \sin^2(\theta/2)}\cos(\theta(m - nq))\mathrm{d}\theta. \tag{3.6}$$

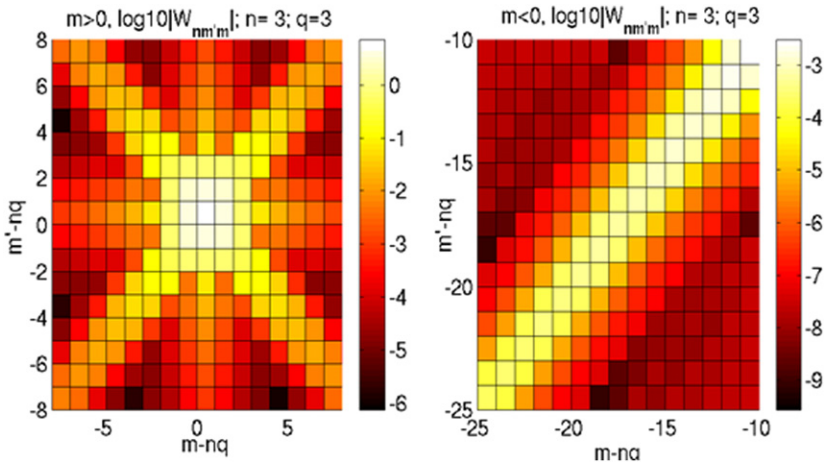

Figure 5. Weighting coefficients for the $1/\nu$ regime calculated using (3.6) for DIII-D #124477 parameters for resonant harmonics (left) and non-resonant harmonics (right) for $q = 3$, $n = 3$.

The complete elliptic integrals of the first and second kind are defined as

$$E(k) = \int_0^{\pi/2} (1 - k^2 \sin^2\theta)^{1/2} \mathrm{d}\theta,$$

$$K(k) = \int_0^{\pi/2} (1 - k^2 \sin^2\theta)^{-1/2} \mathrm{d}\theta.$$

The typical view of the weighting coefficients for resonant and non-resonant harmonics $W_{nmm'}$ in the $1/\nu$ regime is shown in figure 5 for DIII-D coils and plasma parameters. The perturbation spectrum $|b^{\mathrm{H}}_{nm}|$ (3.5) in the Hamada coordinates for DIII-D and ITER parameters and coils is presented in figure 6. The characteristic frequencies for ions and electrons for DIII-D and ITER plasma parameters are presented in figure 7. Here we used parameters $A = 2$; $Z_{\mathrm{i}} = 1$; $\ln\Lambda = 17$. Note that for electrons (figure 7), $q\omega_E < \nu_{\mathrm{e}}/\varepsilon < \sqrt{\varepsilon}\omega_{\mathrm{te}}$ but apart from plasma edge, $q\omega_E > \nu_{\mathrm{i}}/\varepsilon$ both for DIII-D and ITER parameters, and hence the 'ν' regime is expected [13] at least in the central plasma region.

For the ν regime we used the expressions introduced in [14] with corrections due to the special treatment of the boundary between trapped and passing particles compared with the previous studies [11–13]:

$$F_{\mathrm{NTV}} = -\nu_\nu^{\parallel} b_\nu^2 \left(V_\varphi - V_\nu^{\mathrm{NC}}\right), \tag{3.7}$$

$$\nu_\nu^{\parallel} = \nu_{\mathrm{i}}\omega_{\mathrm{ti}}^2/\omega_{\mathrm{E}}^2,$$

$$V^{\mathrm{NC}}_{\nu\,(\mathrm{m\,s^{-1}})} = 0.92/\left(Z_{\mathrm{i}} B_\theta\right)\left(\mathrm{d}T_{\mathrm{i,keV}}/\mathrm{d}r\right), \tag{3.8}$$

$$b_\nu^2 = \sum_{n>0,m,m'=\pm\infty} \left(b_{nmc} b_{nm'c} + b_{nms} b_{nm's}\right) W^{(1)}_{nmm'}.$$

The corresponding weighting coefficients,

$$W^{(1)}_{nmm'} = 0.045\varepsilon^{-1/2} \int_0^1 \mathrm{d}k^2 [E(k) - (1-k^2)K(k)] \times \left(\frac{\partial L^{(1)}_{nm}}{\partial k^2}\frac{\partial L^{(1)}_{nm'}}{\partial k^2} + \frac{\partial L^{(2)}_{nm}}{\partial k^2}\frac{\partial L^{(2)}_{nm'}}{\partial k^2}\right), \tag{3.9}$$

are presented in figure 8.

Here

$$L^{(1)}_{nm} = D_{nm}\frac{(1 - \mathrm{e}^{-\sigma(1-k^2)})\cos(\sigma(1-k^2))}{K(k)},$$

$$L^{(2)}_{nm} = D_{nm}\frac{\mathrm{e}^{-\sigma(1-k^2)}\sin(\sigma(1-k^2))}{K(k)}, \tag{3.10}$$

$$D_{nm} = -2\left\{\int_0^{\pi/2} \frac{\cos\left[(m - nq)\theta(u)\right]\mathrm{d}u}{\sqrt{1 - k^2\sin^2(u)}}\right\},$$

$$\theta(u) = 2\arcsin(k\sin(u)), \qquad \sigma \approx \sqrt{n}\left(\frac{\nu_{\mathrm{d}}}{\ln(16/\sqrt{\nu_{\mathrm{d}}})}\right)^{-1/2},$$

$$\nu_d \approx \frac{4\nu_{\mathrm{i}}}{\varepsilon\omega_E q}.$$

The NTV damping time as $t_{\mathrm{dam}} \approx V_\varphi/(\nu^{\parallel}_{\mathrm{eff}} b^2_{\mathrm{eff}}[V_\varphi - V^{\mathrm{NC}}_*])$ is presented in figure 9 showing that the experimentally measured damping time is closer to the $1/\nu$ regime in DIII-D, and NTV damping time in the ν regime is at least two orders of magnitude larger. Note, however, that vacuum fields were used here and plasma response such as RMP amplification or screening were not taken into account. In [19] the NTV estimations were done taking into account 3D ideal plasma response that showed effective amplification of RMP by a factor of 10 compared with the vacuum fields [19]. However, at present the question of the self-consistent NTV modelling with plasma response remains unresolved. For example ideal plasma response to RMPs described in [19] does not include island formation, rotation and diamagnetic effects, which could be important [20]. Resistive MHD modelling suggests RMP screening by toroidal rotation [17, 20] and also RMP screening by drift effects [20], leading generally to the smaller amplitudes of the resonant harmonics if plasma response with rotation is included. However, for the moment resistive MHD modelling in toroidal geometry was done for Lindquist numbers $S = 10^6$–10^7, which is too small compared with the experimental values. More self-consistent modelling of the MHD plasma response to RMPs including toroidal geometry, island formation, plasma rotation and self-consistent and kinetic modelling of NTV, together with further dedicated

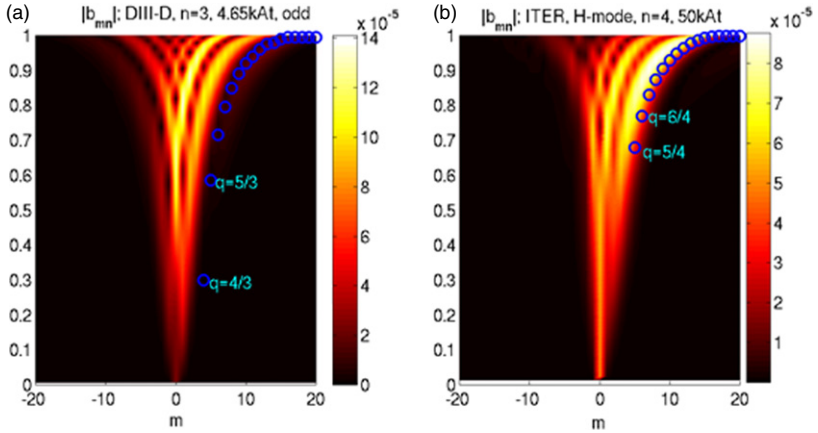

Figure 6. Perturbation strength spectrum in the Hamada coordinates for DIII-D I-coils and equilibrium for #124477 (*a*) and ITER RMP coils and H-mode scenario equilibrium (*b*).

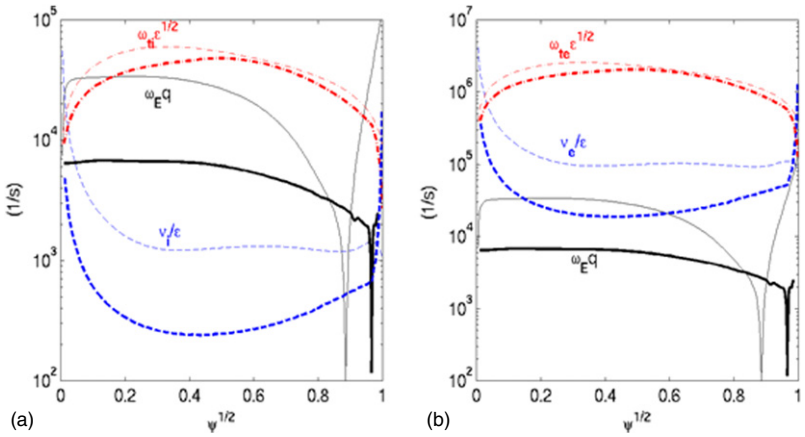

Figure 7. Characteristic transit (dotted–dashed line), collision (dashed line) and toroidal drift frequency (solid line) for ions (*a*) and electrons (*b*) for ITER (in bold) and DIII-D parameters presented in figures 2 and 4.

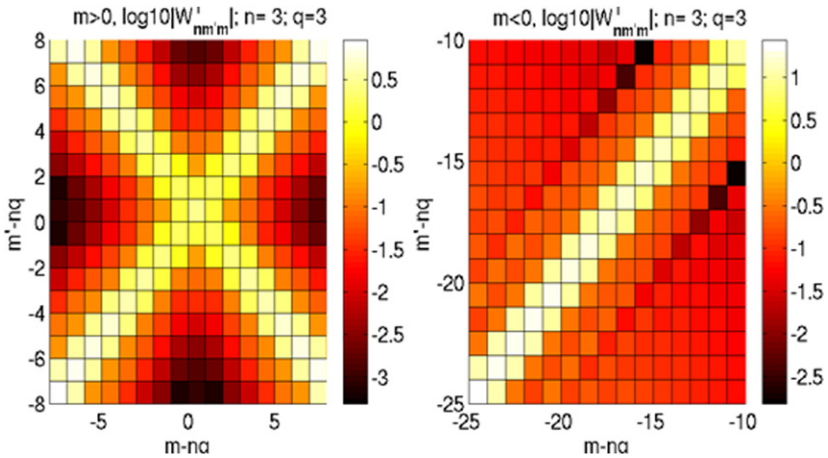

Figure 8. Weighting functions (3.9) in the ν regime for DIII-D #127744 parameters for $q = 3$, $n = 3$; left—$W^{(1)}$ for $m > 0$, right—$W^{(1)}$ for $m < 0$.

experiments on different tokamaks, are still needed for more reliable predictions for ITER and hopefully it will be done in the future. The strategy adopted in this paper was to consider the most pessimistic case with very strong NTV in the $1/\nu$ regime estimated for vacuum fields for ITER.

The flux-averaged profiles of the normalized coefficient $\alpha_{\mathrm{NTV}}(r)$ in (3.1) used in the RMHD code are presented in figure 10. For comparison the typical normalized values of intrinsic perpendicular viscosity were $\nu_{\perp,0} = 0.01$, corresponding to the strong damping of the mean poloidal flow

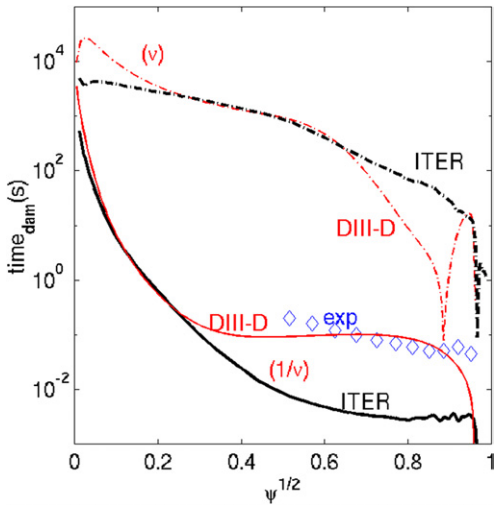

Figure 9. Damping time due to NTV $t_{\rm dam} \approx V_\varphi/(\nu_{\rm eff}^{\parallel} b_{\rm eff}^2 [V_\varphi - V_*^{\rm NC}])$ in DIII-D 127744 and ITER (bold); Dashed–dotted: ν regime, solid: $1/\nu$ regime.

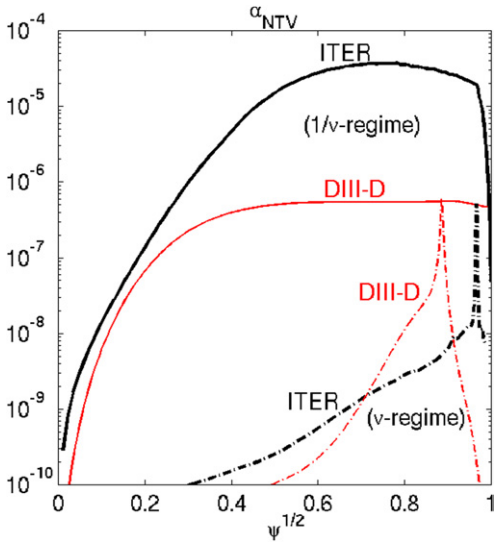

Figure 10. Normalized coefficient due to NTV in (3.1) used in the RMHD code estimated for vacuum fields. For comparison the normalized natural parallel viscosity in modelling was taken as $\nu_{\parallel,0,\rm DIII\text{-}D} = 4.4 \times 10^{-7}$, $\nu_{\parallel,0,\rm ITER} 7.7 \times 10^{-8}$, corresponding to the physical value of $\sim 1 \mathrm{m}^2\,\mathrm{s}^{-1}$.

[6–8], and $\nu_{\parallel,0,\rm DIII\text{-}D} = 4.4 \times 10^{-7}$, $\nu_{\parallel,0,\rm ITER} = 7.7 \times 10^{-8}$ corresponding to the physical natural parallel viscosity of $\sim 1\,\mathrm{m}^2\,\mathrm{s}^{-1}$ which is a typical experimental value.

4. RMHD modelling results

The first step in this study was to estimate numerically the single resonant harmonic penetration without rotation. The resulting flux perturbation $|\psi_{n=-3,m=9}|$ on the surface $q_{(r=0.9)} = |m/n|$ versus time is presented in figure 11(*a*) for different plasma resistivities (here is a constant). The time dependence of the resonance harmonic amplitude $|\psi_{n=-3,m=9}|$ can be fitted by $\psi_{nm}^{\rm pl} \approx \psi_{nm}^{\rm vac}(1 - 0.99\mathrm{e}^{-t/\tau})$. At the boundary magnetic flux perturbation is set to the vacuum value and constant in time: $\psi_{nm}^{\rm vac}(t, r = 1) = 2 \times 10^{-4}$. The dependence of penetration time τ on the normalized resistivity is presented in figure 11(*b*). The fit $\tau/\tau_{\rm A} \sim 1.6 \times 10^{-3}/\eta$ is indicated in figure 11(*b*) by stars. Here the normalized resistivity $\eta = \tau_{\rm A}/\tau_{\rm res} \equiv S^{-1}$, $\tau_{\rm res} = \mu_0 a^2/\eta^{\rm ph}$ is the resistive time and $\eta^{\rm ph} = 1.65 \times 10^{-9} \ln\Lambda Z_{\rm eff} T_{\rm e,keV}^{-3/2}$. According to this scaling for the top of the pedestal of ITER the penetration time for RMP can be roughly estimated as $\tau \sim 1500$ ms ($T_{\rm e} = 4$ keV, $\tau_{\rm A} = a\sqrt{\mu_0\rho_0}/B_0 \sim 3.10^{-7}$ s, $Z_{\rm eff} = 1.5$) and $\tau \sim 50$ ms for DIII-D parameters ($T_{\rm e} = 2$ keV, $\tau_{\rm A} \sim 1.58 \times 10^{-7}$ s, $Z_{\rm eff} = 1.5$).

In the following modelling more realistic resistivity profile was used: $\eta = \eta_{\rm pl}\eta_{\rm vac}/(\eta_{\rm pl} + \eta_{\rm vac})$, $\eta_{\rm vac} = 0.1$, $\eta_{\rm pl} = \eta_0 (p/p_0)^{-3/2}$ which mimics the $\sim T_{\rm e}^{-3/2}$ dependence. Usually with such a profile penetration time roughly decreases by a factor of $\sim$2 compared with figure 11(*b*) estimations, since the edge resistivity is higher compared with the constant value taken for figure 11, but the scaling trend remains. The pressure profile was typical for the H-mode scenario with edge transport barrier for $r > 0.9$. The rotation profile is parabolic with a central value $V_z(r = 0) = V_0$ and zero value at the edge, $V_z(r = 1) = 0$.

The scans of rotation and resistivity showed that screening of magnetic island due to the rotation is stronger at stronger rotation (figure 12) and lower resistivity (figure 13) as it was expected from theory [6, 7, 17]. These results (figures 12 and 13) confirm at least for single harmonics the predictions from [6] for the *visco-resistive* linear regime: $\psi_{mn}^{\rm pl}/\psi_{mn}^{\rm vac}|_{\rm res} \sim \eta^{5/6}/V_0$. Note that in practice with non-constant resistivity profile and strong non-linearity with many harmonics especially in the ergodic zone, this simple scaling is not valid anymore [21], but this trend remains. Note in figure 14 that RMP is screened mainly after resonance surface $\psi_{mn}^{\rm pl} \approx 0$ for $r < r_{\rm res}$. The corresponding current perturbation profiles with and without rotation are presented in figure 15. These results are very similar to those published in [7, 17]. The physical reason for screening is the current layer formation in the narrow region near the resonant surface preventing reconnection and island formation. However, this is valid up to a certain threshold RMP amplitude for reconnection [6].

The 'screening' by rotation applies only to the resonant harmonics ($q = |m/n|$), producing in principle magnetic islands on the resonant surfaces. The non-resonant harmonics (not producing islands since $q \neq |m/n|$) are not affected by rotation. Their amplitude remains the same as in the vacuum case with and without rotation (figure 16). As one can see from figures 16(*a*) and (*b*), the non-resonant harmonic amplitude (here $n = -3$, $m = 2$, $\psi_{mn}(t, r = 1) = 2 \times 10^{-4}$ oscillates during a few hundred Alfvén times due to Alfvén waves, which are then damped depending on the resistivity (stronger damping for higher resistivity—figures 16(*a*) and (*b*)). Note from the Poincaré plot in figure 16(*c*) that no central islands (possible seed islands that trigger NTMs) are produced by non-resonant harmonics, but being a helical perturbation of the equilibrium field they still produce NTV and should be taken into account in rotation profile predictions with RMP coils.

The magnetic topologies from the field line integration [4] done after the run of RMHD code with and without rotation and without NTV ($F_{\rm NTV} = 0$) are presented in figure 17. Here the RMP spectrum applied at the boundary ($r = 1$)

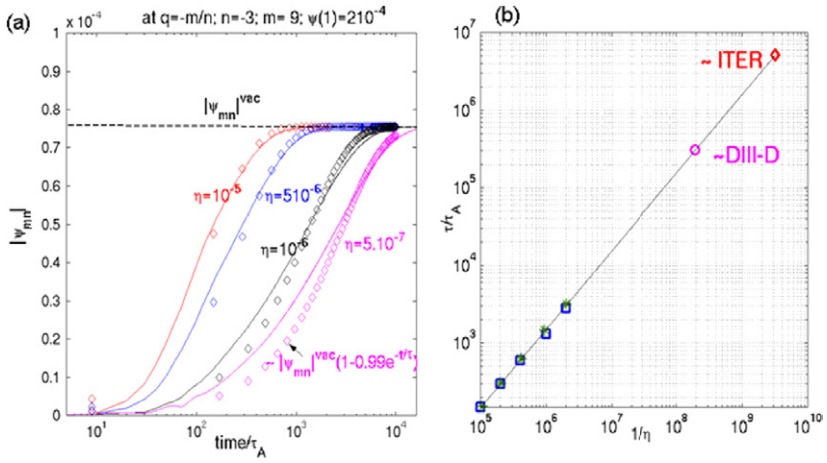

Figure 11. (*a*) Time dependence of resonant harmonic $m = 9$, $n = -3$ flux perturbation amplitude resonant at $r \sim 0.9$ for different resistivities (here constant); fit $\psi_{nm}^{\rm pl} \approx \psi_{nm}^{\rm vac}(1 - 0.99{\rm e}^{-t/\tau})$ is indicated by diamonds. (*b*) Normalized RMP penetration time to the top of the pedestal ($r \sim$0.9) of the harmonic $m/n = 9/3$ as a function of $S = \eta$ (squares); the fit $\tau/\tau_{\rm A} \sim 1.6 \times 10^{-3}/\eta$ is indicated by stars.

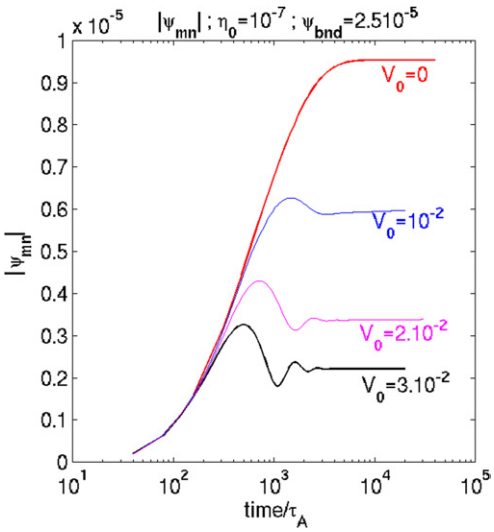

Figure 12. Time dependence of single harmonic amplitude $|\psi_{n=-3,m=9}|$ on the resonance surface $r_{\rm res} = 0.9$ in the rotation V_0 (normalized to $V_{\rm A}$) scan.

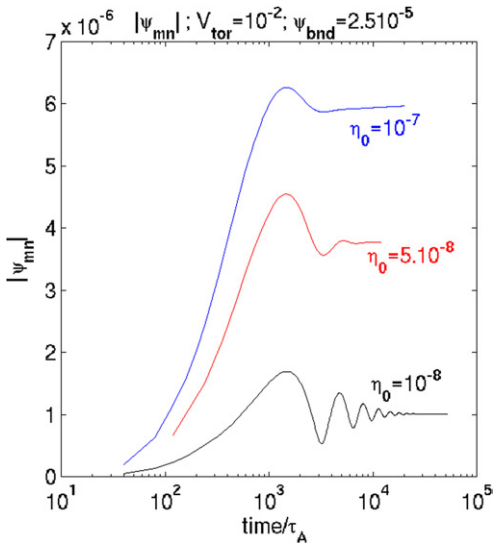

Figure 13. Time dependence of $|\psi_{n=-3,m=9}|$ on $r_{\rm res} = 0.9$ in the resistivity scan at $V_0 = 10^{-2} V_A$.

was $\psi_{n,m=5:11}(r = 1) = [9_{m=5}; 8_{m=6}; \ldots 3_{m=11}] \times 10^{-5}$, $n = -3$. Note that without rotation the edge region is ergodic approximately for $r > 0.9$ and $V_0 = 3 \times 10^{-2}$ ($\sim$10 kHz), $\eta_0 = 10^{-8}$ corresponding to the 'DIII-D-like' and $V_0 = 0.56 \times 10^{-2}$ ($\sim$1 kHz) $\eta_0 = 10^{-9}$ corresponding to the 'ITER-like' parameters [24]. One can see that in both cases the central islands are screened, but still overlap for $r > 0.9$. Finally, the RMHD code runs were done for DIII-D and ITER parameters with NTV calculated in realistic geometry and realistic RMP coils in section 3. It is clear that effect produced by RMPs on the toroidal rotation depends on the relative value of NTV compared with the intrinsic toroidal viscosity $\alpha_{\rm NTV}/\nu_{\|,0}$ and source of rotation itself, for example NBI. Typically in the RMHD modelling we used intrinsic normalized viscosities: $\nu_{\perp,0} = 0.01$, $\nu_{\|,0,\rm DIII\text{-}D} = 4.4 \times 10^{-7}$ and $\nu_{\|,0,\rm ITER} = 7.7 \times 10^{-8}$ (see section 3). The NTV in the ν regime (figure 10) does not produce any noticeable rotation braking in the RMHD modelling at this level of natural viscosity and hence these results are not presented here. In contrast, in the $1/\nu$ regime NTV is rather strong compared with the natural viscosity and will be the dominant mechanism defining the plasma rotation profile, especially in ITER, because of much lower collisionality and lower intrinsic toroidal rotation compared with the present day machines [24]. According to theory [11–14] and experiment [10], the consequence of strong NTV combined with relatively slow or zero toroidal rotation is a counter toroidal rotation with a velocity of $V_\varphi \approx V_*^{\rm NC}$. In contrast, at strong co- or counter rotation global plasma braking is expected as it was observed on DIII-D [10]. This suggests that the resulting value and the direction of the toroidal rotation depend on the interplay between rotation source, the value of NTV and the natural parallel viscosity.

Full RMHD modelling of toroidal rotation profile evolution with $1/\nu$ NTV regime in ITER ($n = -4$, $m = 8 : 14$, $\psi^{nm}(r = 1) = 3.5 \times 10^{-5}$, $\eta(0) = 10^{-9}$, $\nu_{0,\|} = 7.7 \times 10^{-8}$, $\alpha_{\rm NTV,max} = 3.7 \times 10^{-5}$) is presented in figure 18(*a*). Note that in $1/\nu$ regime NTV is strong in ITER with RMPs:

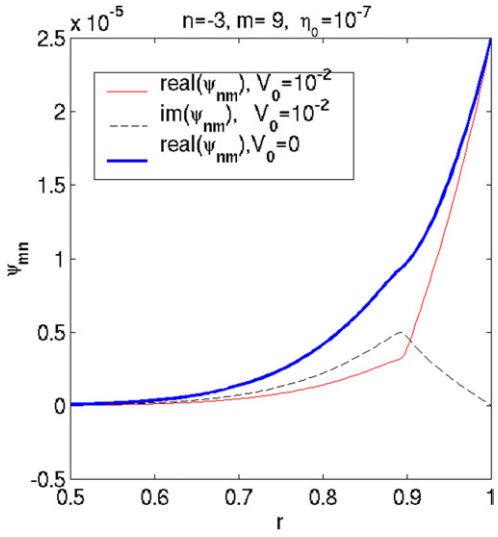

Figure 14. Resonant harmonic $n = -3$, $m = 9$ amplitude profile of the poloidal magnetic flux perturbation at zero rotation $V_0 = 0$ and with rotation $V_0 = 10^{-2} V_A$.

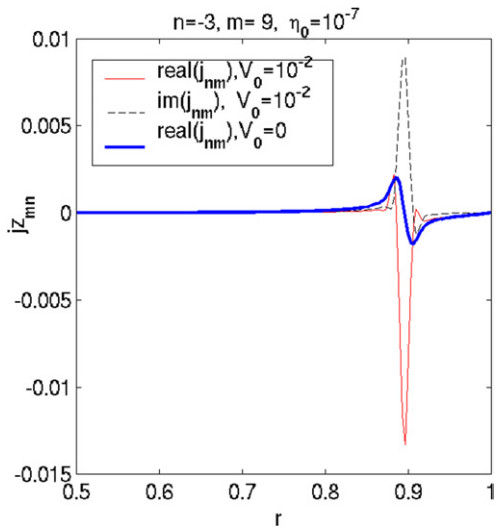

Figure 15. Similar to figure 14, but for the parallel current perturbation harmonic amplitude.

$\alpha_{\mathrm{NTV,max}}/\nu_{||,0} \gg 1$ (figure 10). For comparison rotation profile with only resonant braking is presented in figure 18(*a*) showing very small braking near the resonant surfaces in the ergodic region at the edge. Since NTV is the dominant mechanism here, the simplified equation for toroidal rotation velocity could help to capture the general trend of toroidal rotation behaviour with NTV:

$$\partial v_z/\partial t \approx \delta \cdot S_v + \nu_{||,0}\nabla^2 v_z - \alpha_{\mathrm{NTV,max}} f(r)(v_z - V_{1/\nu}^{\mathrm{NC}}). \quad (4.1)$$

For the general case we introduced in (4.1) a parameter δ which indicates the direction of the intrinsic rotation and $f(r)$ which represents the form of the NTV profile normalized to the maximum value calculated in section 3 and presented in figure 10: $\alpha_{\mathrm{NTV}}(r) = \alpha_{\mathrm{NTV,max}} \cdot f(r)$. For the standard case with the co-neutral beam injection $\delta = 1$. Solving the simplified equation (4.1) for strong NTV permits reducing significantly the time consuming numerical solution (2.1)–(2.4) with a typical time step of $\sim 0.1\tau_{\mathrm{A}}$ until the stationary rotation profile is reached ($\sim 2 \times 10^6 \tau_{\mathrm{A}}$). The profile evolution resulting from (4.1) and RMHD modelling (2.1)–(2.4) with strong NTV ($\alpha_{\mathrm{NTV,max}}/\nu_{||,0} \gg 1$) is very close (figure 18(*a*)) especially in the region of maximum of F_{NTV}. Note that the stationary rotation with NTV in the $1/\nu$ regime for ITER-like parameters presented in figure 18(*b*) is in the counter direction (here negative) and close to the neoclassical value where NTV profile has a maximum, as predicted in [11–13]. The magnetic topology resulting from the full RMHD modelling with NTV due to ITER RMP coils (figure 3) is presented in figure 19 at different times (in τ_{A}) One can see that screening of RMPs is independent of the direction of the rotation (co- or counter) (figure 19); however, the central islands can grow when locally $V_\varphi \sim 0$.

Similar to these numerical results, a spin-up in the counter direction was experimentally observed on DIII-D with the I-coils at slow intrinsic co- or counter rotation obtained by changing the ratio between co- and counter neutral beam injected power [10]. To test this fact, the simplified equation (4.1) was solved numerically with NTV calculated for DIII-D #124477 shot (figure 10) in the $1/\nu$ regime for vacuum fields with parameters $\nu_{0,||} = 7.7 \times 10^{-7}$, $\alpha_{\mathrm{NTV,max}} = 5.5 \times 10^{-7}$, and parabolic initial rotation profile with central value for $\delta = 1$ of $V_0 = 4 \times 10^{-2} V_{\mathrm{A}}$, $V_{\mathrm{A}} \sim 3.8 \times 10^6\,\mathrm{m\,s^{-1}}$, which is close to the experimental conditions of [10]. The time dependence of the toroidal rotation at fixed radius ($r = 0.7$) is presented in figure 20 for different fractions of co- ($\delta > 0$) and counter rotation ($\delta < 0$) and is qualitatively similar to the experimental measurements presented in figure 1 in [10].

5. Conclusions and discussion

The MHD toroidally rotating plasma response to RMPs was estimated. The effective screening of the central magnetic islands by plasma rotation and the pedestal region ergodization are predicted for DIII-D and ITER parameters and the corresponding RMP coils.

Resonant ($q = m/n$) harmonic penetration time at zero rotation increases for lower resistivity and is estimated for a single island ($n = 3$, $m = 9$, resonant at $r \sim 0.9$) to be $\sim$50 ms for DIII-D and $\sim$1500 ms for ITER pedestal parameters. The non-resonant helical harmonics ($q \neq m/n$) in the RMP spectrum are not influenced by plasma rotation and they play an essential role in the NTV mechanism.

If the $1/\nu$ NTV low collisionality regime [11–13] is dominant in ITER, counter rotation close to the neoclassical estimations [13] is predicted for ITER similar to DIII-D observations at slow intrinsic rotation reported in [10]. Both co- and counter toroidal rotations result in central islands screening. Further experimental validation and NTV modelling including MHD rotating plasma response is certainly needed for more reliable predictions of the rotation profile in ITER with RMP coils. Resonant toroidal rotation braking is localized near resonant surfaces similar to [7, 8] and is predicted to be small compared with the $1/\nu$ NTV mechanism for typical DIII-D and ITER parameters used here.

Further development of the model should include diamagnetic effects that represent another important factor

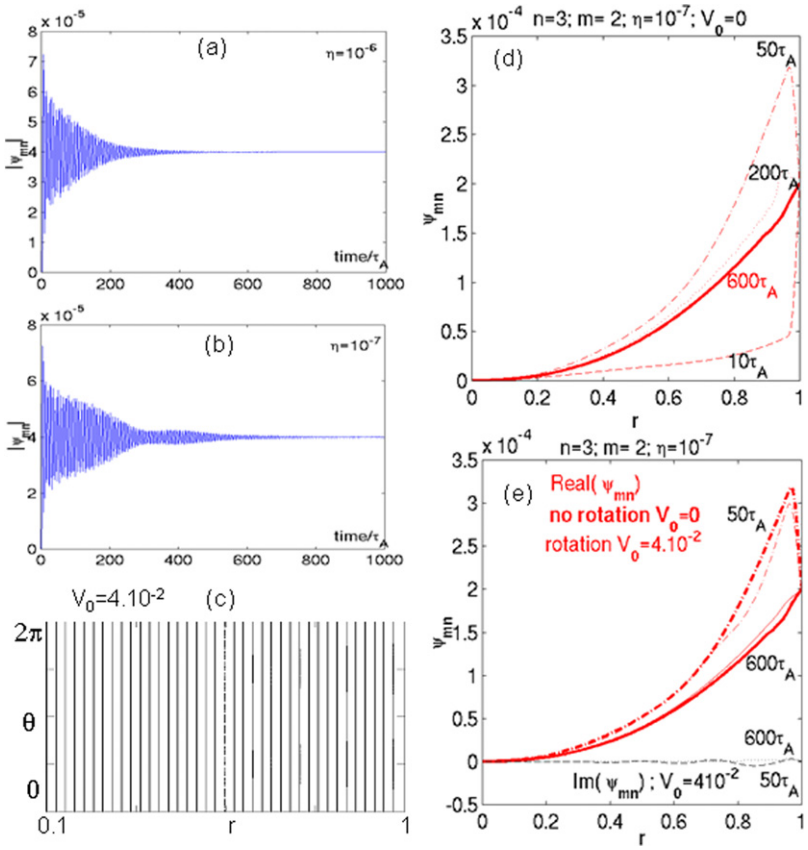

Figure 16. Penetration of non-resonant harmonic $n = -3$, $m = 2$, $\psi_{mn}(1) = 2 \times 10^{-4}(q(0) > 2/3)$ for comparison with figures 11–13. Time dependence of the magnetic flux perturbation at $r = 0.5$ without rotation for $\eta = 10^{-6} = \text{const}$ (a) and $\eta = 10^{-7}$ (b). One can note the oscillations due to Alfvén waves. (c) Poincaré plot of the same with (presented here) and without rotation. No islands are formed since $q \neq m/n$. (d)$\psi_{mn}(r)$ profiles at different times for $\eta = 10^{-7}$ without rotation before stationary vacuum-like solution is reached at $\sim 600\tau_A$ (in bold); (e) profiles $\psi_{mn}(r)$ with and without rotation for non-resonant harmonic are similar.

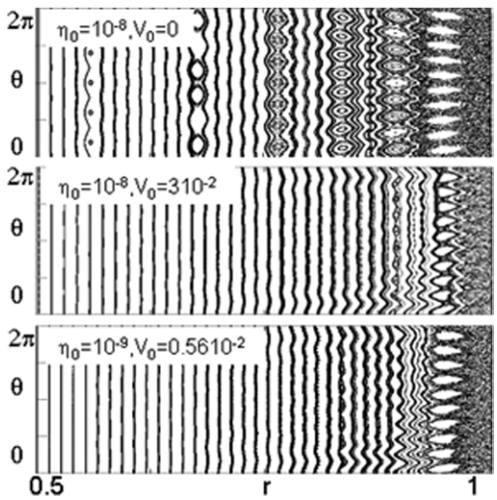

Figure 17. Magnetic topology by field line integration after RMP penetration with RMP spectrum at the boundary $\psi_{n=3,m=5:11}(r = 1) = [9_{m=5}; 8_{m=6}; \ldots 3_{m=11}] \times 10^{-5}$ without rotation (top), with DIII-D-like (middle) and ITER-like (bottom) resistivity and rotation profiles (here without NTV).

for the additional screening of RMP at the edge [20, 22], realistic toroidal geometry and resistive ballooning modes [20], permitting modelling non-linear behaviour ELMs in the presence of RMPs, which was impossible in the cylindrical MHD code, since only current instabilities could be modelled here.

Appendix. Calculation of RMP spectrum in the Hamada coordinates

The magnetic flux coordinates system usually used for RMPs spectrum calculations in [4] was (s, θ, φ) where $s \equiv (\psi^{\mathrm{N}}_{\mathrm{pol}})^{1/2}$, φ is the geometrical toroidal angle and θ is such that, along a field line $\varphi - q\theta = \text{cte}$. Equilibrium field is $\vec{B}_{\mathrm{eq}} = I\nabla\varphi + \nabla\psi \times \nabla\varphi$. Note that in this system for equilibrium field $(\vec{B}_{\mathrm{eq}}, \nabla s) = 0$ and the magnetic lines are straight on the magnetic surface:

$$\frac{B^{(3)}_{\mathrm{eq}}}{B^{(2)}_{\mathrm{eq}}} = \frac{\left(\vec{B}_{\mathrm{eq}}, \nabla\varphi\right)}{\left(B_{\mathrm{eq}}, \nabla\theta\right)} = q(s), \qquad \left(\vec{B}_{\mathrm{eq}}, \nabla\varphi\right) = \frac{I}{R^2}. \quad \text{(A.1)}$$

To use [11–14] for NTV calculations one needs to calculate the RMP magnetic perturbation strength spectrum in the Hamada coordinates. This procedure is given here.

Let us introduce the Hamada coordinates $(V^{\mathrm{H}}, \theta^{\mathrm{H}}, \zeta^{\mathrm{H}})$ [22], where V^{H} is the volume within the flux surface, θ^{H} is the poloidal-like angle and ζ^{H} is the toroidal coordinate. By definition [23]

$$\nabla V^{\mathrm{H}} \times \nabla\theta^{\mathrm{H}} \cdot \nabla\zeta^{\mathrm{H}} = 1. \quad \text{(A.2)}$$

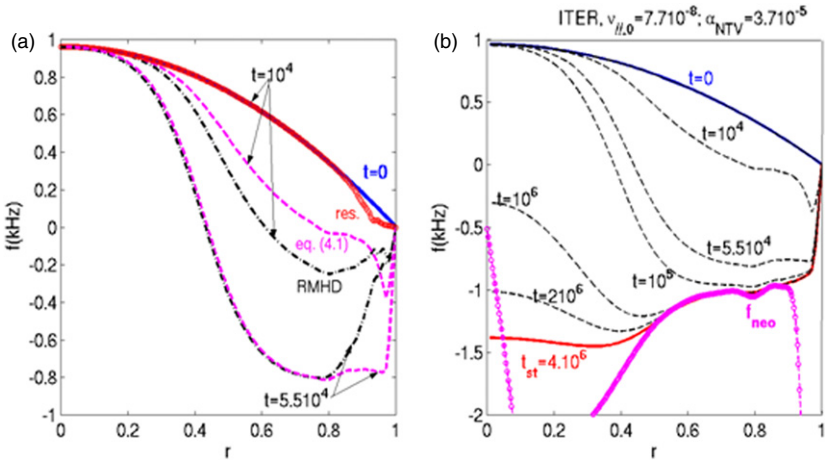

Figure 18. Rotation profile evolution in time due to RMP coils in ITER $n = 4$, 50 kAt. (*a*) Comparison between RMHD code resonant braking only (circles), NTV braking modelled by simplified equation (4.1) (dashed) and RMHD code with NTV (dashed–dotted). (*b*) Toroidal rotation profile evolution from co- to counter direction due to NTV obtained using (4.1) model. Stationary profile is reached at $t \sim 4 \times 10^6 \tau_A$; here $f_{neo} = V_{1/\nu}^{NC}/(2\pi R_0)$.

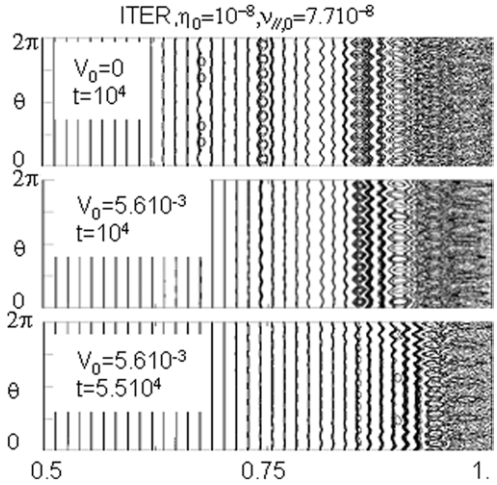

Figure 19. Magnetic topology from RMHD code with NTV estimated in the $1/\nu$ regime for ITER RMP coils at $n = 4$, and maximum current 50 kAt without rotation (top) and with ITER-like rotation at different times (in τ_A) . One can note that both co- and counter rotations screen central islands, and that the islands can increase their size if toroidal rotation is locally close to zero (for example islands on $q = m/n$ =11/4 surface at $t = 104\tau_A$).

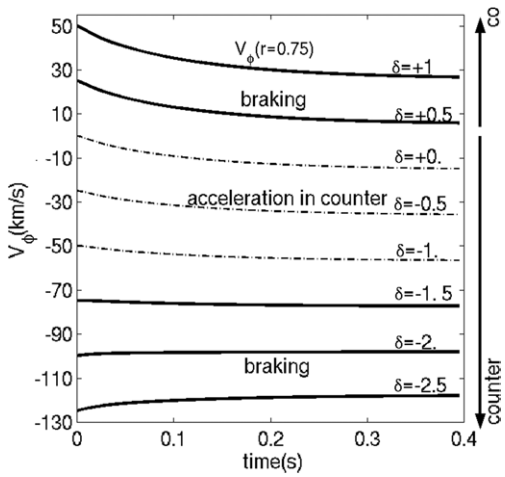

Figure 20. The time evolution of toroidal velocity at $r = 0.75$ from numerical solution of equation (4.1) with DIII-D-like parameters and parabolic initial rotation profile with a central value $V_0 = 3 \times 10^{-2} V_A$, $V_A \sim 3.8 \times 10^6$ m s^{-1} and $\alpha_{NTV}(r)$ form shown in figure 10 for DIII-D #124477 shot and for different fractions of co- ($\delta > 0$) and counter rotation ($\delta < 0$). Here normalized values are $\nu_{0,\|} = 4.4 \times 10^{-7}$, $\alpha_{NTV,max} = 5.5 \times 10^{-7}$.

The equilibrium field in the Hamada coordinates is expressed as

$$\vec{B}_{eq} = \nabla V^H \times \left(\psi^H \nabla\theta^H - \chi^H \nabla\zeta^H\right), \qquad \psi^H = \vec{B}_{eq} \cdot \nabla\theta^H,$$
$$\chi^H = \vec{B}_{eq} \cdot \nabla\zeta^H. \tag{A.3}$$

Note that in the Hamada coordinates (V^H, θ^H, ζ^H), as also in the (s, θ, φ) system, the magnetic lines are straight and the 'radial' (perpendicular to the flux surface) component is zero:

$$\frac{\left(\vec{B}_{eq}, \nabla\zeta^H\right)}{\left(B_{eq}, \nabla\theta^H\right)} = q\left(V^H\right) \equiv q(s), \qquad \left(\vec{B}_{eq}, \nabla V^H\right) = 0. \tag{A.4}$$

The volume enclosed by a flux surface V^H can be expressed as $V^H(s) = 2\pi \int_{s=0}^{s} \int_{\theta=0}^{2\pi} R \mathrm{d}S$, where $\mathrm{d}S$ is the appropriate surface element. Since V^H is the volume within a flux surface; in the following we use 's' still as a label of the flux surface. For the poloidal Hamada angle we can chose the following expression:

$$\theta^H = \frac{\int_0^\theta \mathrm{d}\theta / \left(\vec{B} \cdot \vec{\nabla}\theta\right)}{\int_0^{2\pi} \mathrm{d}\theta / \left(\vec{B} \cdot \vec{\nabla}\theta\right)}. \tag{A.5}$$

The second Hamada angle can be constructed according to

$$\zeta^H = \frac{\varphi}{2\pi} + \frac{I}{2\pi} \int_0^\theta \left(\mathrm{d}\theta / \underbrace{\vec{B} \cdot \vec{\nabla}\theta}_{=B^{(2)}} \right) \cdot \left(\left\langle \frac{1}{R^2} \right\rangle - \frac{1}{R^2} \right)$$
$$= \frac{\varphi}{2\pi} + \frac{1}{2\pi} \int_0^\theta \mathrm{d}\theta \frac{\left(\left\langle B^{(3)} \right\rangle - B^{(3)}\right)}{B^{(2)}}$$
$$= \frac{\varphi}{2\pi} + \frac{\left\langle B^{(3)} \right\rangle}{2\pi} \left(\int_0^\theta \frac{\mathrm{d}\theta}{B^{(2)}} \right) - \frac{1}{2\pi} \left(\int_0^\theta \frac{B^{(3)}}{B^{(2)}} \mathrm{d}\theta \right)$$

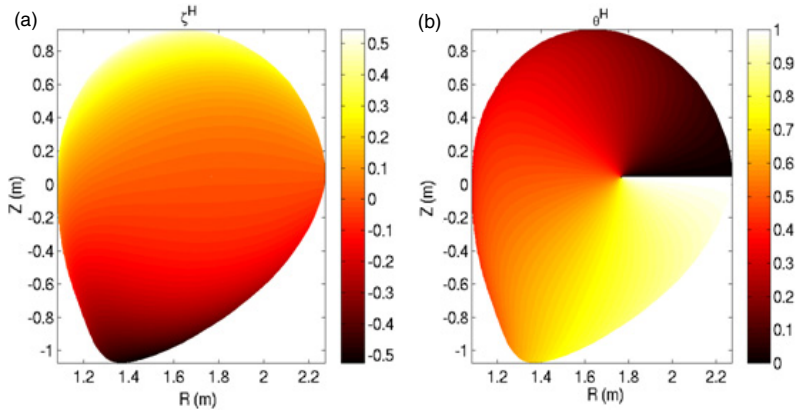

Figure 21. (*a*) Hamada toroidal angle $\zeta^{\mathrm{H}} = \zeta_{\mathrm{H}}(s, \theta, \varphi = 0)$ and (*b*) Hamada poloidal angle $\theta^{\mathrm{H}} = \theta^{\mathrm{H}}(s, \theta, \varphi = 0)$ for DIII-D #127744 shot equilibrium at zero toroidal geometrical angle.

$$= \frac{\varphi}{2\pi} + \frac{1}{2\pi}\frac{\int_0^{2\pi}\frac{B^{(3)}}{B^{(2)}}\mathrm{d}\theta}{\int_0^{2\pi}\frac{1}{B^{(2)}}\mathrm{d}\theta}\left(\int_0^{\theta}\frac{\mathrm{d}\theta}{B^{(2)}}\right) - q\frac{\theta}{2\pi}$$

$$= \frac{\varphi}{2\pi} + q\frac{\left(\int_0^{\theta}\frac{\mathrm{d}\theta}{B^{(2)}}\right)}{\int_0^{2\pi}\frac{1}{B^{(2)}}d\theta} - q\frac{\theta}{2\pi} = \frac{1}{2\pi}\varphi$$

$$+ q\left(\theta^{\mathrm{H}} - \frac{1}{2\pi}\theta\right). \tag{A.6}$$

Here we used the definition of flux averaging as

$$\left\langle \frac{I}{R^2}\right\rangle = \left\langle B^{(3)}\right\rangle = \frac{\int_0^{2\pi} B^{(3)}\cdot\left(\mathrm{d}\theta/\vec{B}\cdot\vec{\nabla}\theta\right)}{\int_0^{2\pi}\mathrm{d}\theta/\vec{B}\cdot\vec{\nabla}\theta}. \tag{A.7}$$

The final expression linking our flux coordinates (s, θ, φ) with Hamada is

$$\zeta_{\mathrm{H}}(s,\theta,\varphi) - q\theta_{\mathrm{H}}(s,\theta) = \frac{1}{2\pi}(\varphi - q\theta).$$

We chose $\theta = 0$, $\theta^{\mathrm{H}}|_{\theta=0} = 0$ on the low field side (LFS) mid-plane. The Hamada angles $\zeta^{\mathrm{H}} = \zeta_{\mathrm{H}}(s, \theta, \varphi = 0)$ and $\theta^{\mathrm{H}} = \theta^{\mathrm{H}}(s, \theta, \varphi = 0)$ on the equilibrium mesh are illustrated in figure 21.

For convenience of Fourier spectrum calculations, the Hamada angles were normalized as follows, assuming that

$$\tilde{\theta}^{\mathrm{H}} = 2\pi\theta^{\mathrm{H}}(s,\theta), \qquad \tilde{\zeta}^{\mathrm{H}} = 2\pi\zeta^{\mathrm{H}}(s,\theta,\varphi). \tag{A.8}$$

We now want to calculate the coefficients $A_n(\tilde{\theta}^{\mathrm{H}})$, $B_n(\tilde{\theta}^{\mathrm{H}})$ in expression (6) of [11, 12]. Consider that in the first order the magnetic field strength on the field line is

$$B = (\vec{B}_{\mathrm{eq}} + \delta\vec{B}, \vec{B}_{\mathrm{eq}} + \delta\vec{B})^{1/2} \approx \frac{1}{B_{\mathrm{eq}}}(\vec{B}_{\mathrm{eq}}, \vec{B}_{\mathrm{eq}} + \delta\vec{B})$$

$$\approx B_{\mathrm{eq}}(V^{\mathrm{H}}, \theta^{\mathrm{H}}) + \frac{1}{B_{\mathrm{eq}}}(\vec{B}_{\mathrm{eq}}(V^{\mathrm{H}}, \theta^{\mathrm{H}})\cdot\delta\vec{B}(V^{\mathrm{H}}, \theta^{\mathrm{H}}, \zeta^{\mathrm{H}})) \tag{A.9}$$

and approximately as in [11, 12]:

$$B = B_{\mathrm{eq}}\left(1 + \frac{1}{B_{\mathrm{eq}}}\vec{B}_{\mathrm{eq}}\cdot\delta\vec{B}\right) \approx B_{\mathrm{eq}} + B_0\left(\frac{\vec{B}_{\mathrm{eq}}\cdot\delta\vec{B}}{B_{\mathrm{eq}}B_0}\right)$$

$$\equiv B_{\mathrm{eq}} + B_0 b, \tag{A.10}$$

where

$$b = \frac{\vec{B}_{\mathrm{eq}}\cdot\delta\vec{B}}{B_0} \approx \frac{1}{B_0}\left(\frac{B^R_{\mathrm{eq}}\delta B^R}{B_0} + \frac{B^Z_{\mathrm{eq}}\delta B^Z}{B_0} + \frac{B^{\varphi}_{\mathrm{eq}}\delta B^{\varphi}}{B_0}\right).$$

Introducing the label of the magnetic line on the magnetic surface $\zeta^0 = q\tilde{\theta}^{\mathrm{H}} - \tilde{\zeta}^{\mathrm{H}}$ note that $\vec{B}\nabla\zeta^0 = 0$. The Fourier transform of magnetic strength perturbation along the unperturbed field line in the Hamada coordinates can be written in the form

$$b = \sum_{n=\pm\infty, n\neq 0}\sum_{m=\pm\infty} b^{\mathrm{H}}_{nm}\left(s,\tilde{\theta}^{\mathrm{H}}\right)\mathrm{e}^{-\mathrm{i}n\tilde{\zeta}^{\mathrm{H}}+\mathrm{i}m\tilde{\theta}^{\mathrm{H}}}$$

$$= \sum_{n=\pm\infty, n\neq 0}\sum_{m=\pm\infty} b^{\mathrm{H}}_{nm}\left(s,\tilde{\theta}^{\mathrm{H}}\right)\mathrm{e}^{\mathrm{i}\tilde{\theta}^{\mathrm{H}}(m-nq)}\mathrm{e}^{\mathrm{i}n\zeta^0}$$

$$\equiv \sum_{n=\pm\infty, n\neq 0} C_n\mathrm{e}^{\mathrm{i}n\zeta^0}. \tag{A.11}$$

Since b is a real number $C_{-n} = C_n^*$ and b can be represented as

$$b = \sum_{n>0} A_n\cos\left(n\zeta^0\right) + B_n\sin\left(n\zeta^0\right)$$

$$A_n = 2\mathrm{Real}(C_n), \qquad B_n = -2\mathrm{Im}(C_n),$$

$$A_n = \mathrm{Real}\left(b^{\mathrm{H}}_{m=0,n}\mathrm{e}^{\mathrm{i}\tilde{\theta}^{\mathrm{H}}nq} + 2\sum_{m=\pm\infty, m\neq 0} b^{\mathrm{H}}_{mn}\mathrm{e}^{\mathrm{i}\tilde{\theta}^{\mathrm{H}}(m-nq)}\right)$$

$$= \mathrm{Real}\left(b^{\mathrm{H}}_{0n}\right)\cos\left(\tilde{\theta}^{\mathrm{H}}nq\right) - \mathrm{Im}\left(b^{\mathrm{H}}_{0n}\right)\sin\left(\tilde{\theta}^{\mathrm{H}}nq\right)$$

$$+2\sum_{m=\pm\infty}\mathrm{Real}\left(b^{\mathrm{H}}_{mn}\right)\cos\left(\tilde{\theta}^{\mathrm{H}}(m-nq)\right) - \mathrm{Im}\left(b^{\mathrm{H}}_{mn}\right)$$

$$\times\sin\left(\tilde{\theta}^{\mathrm{H}}(m-nq)\right)$$

$$= \sum_{m=\pm\infty} b_{mnc}\cos\left(\tilde{\theta}^{\mathrm{H}}(m-nq)\right) + b_{mns}\sin\left(\tilde{\theta}^{\mathrm{H}}(m-nq)\right),$$

$$b_{mnc} = \begin{cases} 2\mathrm{Real}\left(b^{\mathrm{H}}_{mn}\right), m\neq 0, \\ \mathrm{Real}\left(b^{\mathrm{H}}_{mn}\right), m = 0, \end{cases}$$

$$b_{mns} = \begin{cases} -2\mathrm{Im}\left(b^{\mathrm{H}}_{mn}\right), m\neq 0, \\ -\mathrm{Im}\left(b^{\mathrm{H}}_{mn}\right), m = 0, \end{cases}$$

$$B_n = -\mathrm{Im}\left(b^{\mathrm{H}}_{m=0,n}\mathrm{e}^{\mathrm{i}\tilde{\theta}^{\mathrm{H}}nq} + 2\sum_{m=\pm\infty, m\neq 0} b^{\mathrm{H}}_{mn}e^{\mathrm{i}\tilde{\theta}^{\mathrm{H}}(m-nq)}\right)$$

$$= -\mathrm{Im}\left(b^{\mathrm{H}}_{0n}\right)\cos\left(\tilde{\theta}^{\mathrm{H}}nq\right) - \mathrm{Real}\left(b^{\mathrm{H}}_{0n}\right)\sin\left(\tilde{\theta}^{\mathrm{H}}nq\right)$$

$$-2\sum_{m=\pm\infty,m\neq 0}\mathrm{Im}\left(b^{\mathrm{H}}_{mn}\right)\cos\left(\tilde{\theta}^{\mathrm{H}}(m-nq)\right)$$
$$-\mathrm{Real}\left(b^{\mathrm{H}}_{mn}\right)\sin\left(\tilde{\theta}^{\mathrm{H}}(m-nq)\right)$$
$$=\sum_{m=\pm\infty}b_{mns}\cos\left(\tilde{\theta}^{\mathrm{H}}(m-nq)\right)-b_{mnc}\sin\left(\tilde{\theta}^{\mathrm{H}}(m-nq)\right); \tag{A.12}$$

So for calculating A_n and B_n one should know a spectrum in the Hamada coordinates:

$$b\left(s,\tilde{\theta}^{\mathrm{H}},\tilde{\zeta}^{\mathrm{H}}\right)=\sum_{n=\pm\infty,n\neq 0}\sum_{m=\pm\infty}b^{\mathrm{H}}_{mn}\left(s,\tilde{\theta}^{\mathrm{H}}\right)\mathrm{e}^{-\mathrm{i}n\tilde{\zeta}^{\mathrm{H}}+\mathrm{i}m\tilde{\theta}^{\mathrm{H}}},$$
$$b^{\mathrm{H}}_{mn}=\frac{1}{4\pi^2}\int_0^{2\pi}\int_0^{2\pi}b\left(s,\tilde{\theta}^{\mathrm{H}},\tilde{\zeta}^{\mathrm{H}}\right)\mathrm{e}^{\mathrm{i}(n\tilde{\zeta}^{\mathrm{H}}-m\tilde{\theta}^{\mathrm{H}})}\mathrm{d}\tilde{\zeta}^{\mathrm{H}}\mathrm{d}\tilde{\theta}^{\mathrm{H}}. \tag{A.13}$$

Since $\tilde{\zeta}^{H}(s,\theta,\varphi)=\tilde{\zeta}^{H}(s,\theta,0)+\varphi$, one can write

$$b^{\mathrm{H}}_{mn}=\frac{1}{2\pi}\int_0^{2\pi}\left(\frac{1}{2\pi}\int_0^{2\pi}b_n\cdot\mathrm{e}^{\mathrm{i}n\varphi}\mathrm{d}\varphi\right)\cdot\mathrm{e}^{\mathrm{i}(n\tilde{\zeta}^{\mathrm{H}}_0-m\tilde{\theta}^{\mathrm{H}})}\mathrm{d}\tilde{\theta}^{\mathrm{H}}$$
$$=\frac{1}{2\pi}\int_0^{2\pi}b^*_n\cdot\mathrm{e}^{\mathrm{i}n\tilde{\zeta}^{\mathrm{H}}_0-\mathrm{i}m\tilde{\theta}^{\mathrm{H}}}\mathrm{d}\tilde{\theta}^{\mathrm{H}}, \tag{A.14}$$

where $\tilde{\zeta}^{\mathrm{H}}_0(s,\theta)=\tilde{\zeta}^{\mathrm{H}}(s,\theta,\varphi=0)$ and $b_n=(1/2\pi)\times\int_0^{2\pi}b(s,\tilde{\theta}^{\mathrm{H}},\varphi)\mathrm{e}^{-\mathrm{i}n\varphi}\mathrm{d}\varphi$ designate the traditional Fourier transform with respect to φ for each $\tilde{\theta}^{\mathrm{H}}=$ const . Note that according to our definition of angles here, $b^*_n(s,\theta^{\mathrm{H}})=(1/2\pi)\int_0^{2\pi}b(s,\theta^{\mathrm{H}},\varphi)\mathrm{e}^{\mathrm{i}n\varphi}\mathrm{d}\varphi$. Finally,

$$b^{\mathrm{H}}_{mn}=\frac{1}{2\pi}\int_0^{2\pi}b^*_n\cdot\mathrm{e}^{\mathrm{i}nq(\tilde{\theta}^{\mathrm{H}}-\theta)-\mathrm{i}m\tilde{\theta}^{\mathrm{H}})}\mathrm{d}\tilde{\theta}^{\mathrm{H}}$$
$$=\frac{1}{2\pi}\int_0^{2\pi}b^*_n\mathrm{e}^{\mathrm{i}\tilde{\theta}^{\mathrm{H}}(-m+nq)}\mathrm{e}^{-\mathrm{i}nq\theta}\left(\frac{\partial\tilde{\theta}^{\mathrm{H}}}{\partial\theta}\right)\mathrm{d}\theta. \tag{A.15}$$

Hence the poloidal harmonic amplitude in the Hamada coordinates at each flux surface is calculated as a traditional poloidal Fourier harmonic, but for the phase shifted function $(b^*_n\cdot\mathrm{e}^{\mathrm{i}nq(\tilde{\theta}^{\mathrm{H}}-\theta)})$:

$$b^{\mathrm{H}}_{mn}=\frac{1}{2\pi}\int_0^{2\pi}\mathrm{e}^{-\mathrm{i}m\tilde{\theta}^{\mathrm{H}}}\left(b^*_n\cdot\mathrm{e}^{\mathrm{i}nq(\tilde{\theta}^{\mathrm{H}}-\theta)}\right)\mathrm{d}\tilde{\theta}^{\mathrm{H}}. \tag{A.16}$$

Acknowledgments

The authors would like to thank many colleagues who were involved in the combined theoretical, modelling, experimental and engineering efforts in RMP ELM control coils design for ITER and, in particular, R. Hawryluk, P. Thomas, A. Loarte, V. Chuyanov, D. Campbell, U. Gribov, G. Janeschitz, J.-J. Cordier, D. Losser, Y. Liang, J. Menard, S. Sabbagh, J. Callen. A very special thanks to B. Scott for recommendations for the magnetic perturbation spectrum calculations in the Hamada coordinates that were used here, and to A. Polevoi [24] who provided the expected profiles for ITER standard H-mode scenario used already in [4, 5] and also here.

This work, supported by the European Communities under the contract of Association between EURATOM and CEA, was carried out within the framework of the European Fusion Development Agreement. The views and opinions expressed herein do not necessarily reflect those of the European Commission.

References

[1] Hawryluk R.J. *et al* 2009 *Nucl. Fusion* **49** 065012
[2] Evans T. *et al* 2008 *Nucl. Fusion* **48** 024002
[3] Liang Y. *et al* 2007 *Phys. Rev. Lett.* **98** 265004
[4] Becoulet M. *et al* 2008 *Nucl. Fusion* **48** 024003
[5] Schaffer M. *et al* 2008 *Nucl. Fusion* **48** 024004
[6] Fitzpatrick R. 1998 *Phys. Plasmas* **5** 3325
[7] Kikuchi Y. *et al* 2006 *Plasma Phys. Control. Fusion* **48** 169
[8] Lazzaro E. *et al* 2002 *Phys. Plasmas* **9** 3906
[9] Zhu W. *et al* 2006 *Phys. Rev. Lett.* **96** 225002
[10] Garofalo A. *et al* 2008 *Phys. Rev. Lett.* **101** 195005
[11] Shaing K. 2003 *Phys. Plasmas* **10** 1443
[12] Shaing K 2007 *Phys. Plasmas* **14** 049903 (erratum)
[13] Cole A. *et al* 2008 *Phys. Plasmas* **15** 056102
[14] Shaing K. *et al* 2008 *Phys. Plasmas* **15** 082506
[15] Huysmans G. 2001 *Phys. Rev. Lett.* **87** 245002
[16] Helzeltine R.D. *et al* 1985 *Phys. Fluids* **28** 2466
[17] Nardon E. *et al* 2007 *Phys. Plasmas* **14** 092501
[18] Chang C.S. *et al* 2004 *Phys. Plasmas* **11** 2649
[19] Park J.-K. *et al* 2008 *Proc. 22nd Int. Conf. on Fusion Energy 2008 (Geneva, Switzerland, 2008)* (Vienna: IAEA) CD-ROM file EX/5-3Rb and http://www-naweb.iaea.org/napc/physics/FEC/FEC2008/html/index.htm
[20] Strauss H.R. *et al* 2009 *Nucl. Fusion* **49** 055025
[21] Izzo V.A. *et al* 2008 *Proc. 22nd Int. Conf. on Fusion Energy 2008 (Geneva, Switzerland, 2008)* (Vienna: IAEA) CD-ROM file TH/P4-19 and http://www-naweb.iaea.org/napc/physics/FEC/FEC2008/html/index.htm
[22] Heyn M.F. *et al* 2008 *Nucl. Fusion* **48** 024005
[23] Hamada S. 1962 *Nucl. Fusion* **2** 23
[24] Polevoi A. *et al* 2002 ITER confinement and stability modelling *J. Plasma Fusion Res. Ser.* **5** 82–7